Agrowaste derived biochars impregnated with ZnO for removal of arsenic and lead in water

G.J.F. Cruz[1*], D. Mondal[2], J. Rimaycuna[1], K. Soukup[3], M.M. Gómez[4], J.L. Solis[4], J. Lang[5]

[1]Universidad Nacional de Tumbes, Departamento de Ingeniería Forestal y Gestión Ambiental, Tumbes, Perú.

[2]University of Salford, School of Science, Engineering & Environment, Salford, United Kingdom

[3]Institute of Chemical Process Fundamentals of the CAS, Prague, Czech Republic.

[4]Universidad Nacional de Ingeniería, Facultad de Ciencias, Lima, Perú.

[5]Technical University of Ostrava, Institute of Environmental Technology, Ostrava, Czech Republic.

*Corresponding author: gcruzc@untumbes.edu.pe

Abstract

Using residual biomass for biochar production to be applied for water treatment is a cost effective and environmental-friendly alternative to activated carbon. However, biochars are materials with low textural properties (total specific area and total pore volume) and hence lower adsorption capacity compared to activated carbon. In that sense, this study aimed to impregnate ZnO on biochar derived from agricultural residual biomass to improve its As(V) and Pb(II) adsorption capacity. Biochars derived from corn cob and coffee husk were prepared by carbonization in mild conditions and then impregnated with ZnO using precipitation method. The resulting materials were comprehensively characterized describing their textural, chemical, surface, morphological and structural properties. Adsorption capacity of the produced materials was tested with As(V) and

Pb(II) in kinetic and equilibrium experiments. The ZnO impregnation of the biochars derived from both precursors improves their adsorption capacities and, in most cases, accelerates the rate of adsorption of both pollutants. The best results were obtained by corncob derived ZnO impregnated biochar (CC-ZnO) reaching a maximum equilibrium adsorption capacity of 25.9 mg of As(V)/g and at least 25.8 mg of Pb(II)/g. The corncob derived ZnO impregnated biochar is a suitable adsorbent candidate for the use in the removal of As and Pb from polluted water.

Keywords: corncob, coffee husk, residual biomass, water treatment, adsorption

1. Introduction

The South American climate is suitable for the year-round agricultural production with multiple harvests. Indeed, in Peru, an important agricultural nation, the production of the two major crops- coffee and corn in the year 2018 was 364.6 kilo tonnes and 1262.3 kilo tonnes respectively [1]. The year-round agriculture not only produces large quantities of crops, but also agrowastes. For example, coffee husk and corn cob, are agricultural wastes representing 12 wt% and 85 wt% of the whole raw material respectively [2]. These agrowastes are usually either burned in open fields or dumped without further use. This disposal not only presents a financial burden but also is an increased ecological load and in fact a missed opportunity. The agrowastes can be utilized in the production of materials with added value such as carbonaceous materials - activated carbon [2-4] and biochar [5, 6]. Recent research interests in the synthesis of biochar and its application in the treatment of contaminated soil have resulted in agrowastes regaining the attention for developing sustainable, value-added and eco-friendly product [7]. Traditionally, the activated carbon have been used as an adsorbent, while the biochar have been used for soil amendment and carbon capture and storage [7]. However nowadays, use of biochar instead of activated carbon for water and wastewater treatments offers different environmental advantages. Although biochar is inferior to activated carbon in adsorption capacity, because of lower textural properties, it is easier to manufacture and more environmentally friendly [8]. In order to improve textural properties of carbonaceous adsorbents and thus their adsorption capacity, different strategies have been tested including microwave treatment, acid and base treatment, plasma treatment, and impregnation, among others [9]. Due to non-toxic characteristic, ZnO nanoparticle is commonly used in many environmental and food applications. It is a GRAS compound (generally recognized as safe), and approved by Food and Drugs Administration (FDA),

the federal agency of the United States Department of Health and Human Services for use in food for human consumption [10]. Hence use of ZnO nanoparticle impregnation and use of the derived biochar for drinking water treatment could be considered as a safe option. Besides, others important characteristics are its thermal stability [11] and good adsorption capacity [12]. Not only, the heavy metals adsorption capacity of pure ZnO has been studied [13] but also, the use of impregnated ZnO nanoparticles to improve heavy metals adsorption capacities of different materials have been noted [14-17]. The great affinity of ZnO for positively charged metal ions (such as Pb) has been demonstrated [13-15, 18, 19] and authors often agreed that the mechanism is based on the binding of cations to the surface hydroxyl groups of ZnO [14, 16, 19] with release of protons to the solution. Furthermore, ZnO might have potential active sites for adsorption of metals ions because of its porous structure and surface polar nature of positively charged Zn ion and negatively charged O ion [14]. Adsorption between negatively charged oxyanions (such As(V)) and ZnO, might occur through ligand exchange of the hydroxyl group from Zn-OH to form Zn-O-As complex [17].

Although the use of ZnO to improve activated carbon properties has been studied [16, 20-24], there is limited knowledge on impregnation of ZnO on biochars and its effect on improving the biochar properties. Biochar impregnated with ZnO has been mainly used in photocatalytic activity tests with organic compounds and dyes [25-27] and to a lesser extent in adsorption of heavy metals [28, 29].

The importance of As and Pb removal from water is of great significance since in the Tumbes region, located in north-west of Peru, the irrigation water for the crops coming mainly from the Tumbes river flowing in Peru from Ecuador is often heavily polluted with heavy metals including As and Pb due to contamination from illegal mining activities upstream of the river [30]. In our recent study, it was found that paddy fields located

downstream in the Tumbes river basin could be negatively affected by the irrigation water containing As and Pb resulting in increased human exposure due to soil-crop transfer [31]. Rice is widely known to be a significant route of As exposure [32] due to its high ability to absorb As from the soil [33]. Besides, elevated concentration of Pb in certain rice varieties is also reported [34]. Consumers of rice could be at considerable risk of carcinogenesis due to As and Pb exposure [35]. Hence, treatment of irrigation water to reduce the load of As and Pb can reduce rice contamination and hence exposure.

In this study, biochar derived from both corncob and coffee husk, which are the major local agrowastes in Peru, was synthesized by carbonization at 600 °C during 2 h and comprehensively characterised. The produced biochars were then successfully impregnated with ZnO nanoparticles using precipitation method and the efficacy of the impregnated biochars on the adsorption capacity of As(V) and Pb(II) in aqueous solution was tested.

2. Material and method

2.1. Materials

The agrowastes - coffee husk (CH) and corncob (CC) were obtained from different producers of Tumbes in Peru. The biomasses were dried at 80 °C until constant weight was reached, grounded and sieved to obtain a particle size less than 0.5 mm. The reagents utilized in the synthesis of impregnated biochars were reagent grade sodium hydroxide (NaOH) and zinc nitrate tetrahydrate ($Zn(NO_3)_2.4H_2O$) purchased from Merck (Germany). For adsorption experiments, sodium arsenate dibasic heptahydrate ($Na_2HAsO_4.7H_2O$) from Honeywell Fuka and lead(II) chloride ($PbCl_2$) from Acros Organics reagents grade were used for preparation of As(V) and Pb(II) solutions.

2.2. Production of biochars

The two different biochar materials were produced from coffee husk (CH) and corncob (CC) by pyrolyzing the grounded and sieved (particle size 0.5 mm) biomasses (50 g/batch) at 600 °C with a heating rate of 10 °C/min (Tubular Furnace Naberthem GmbH, Germany, model R 120/500/12), in a flux of 150 mL/min nitrogen (technical grade, purity of 99.5 %) controlled by a multi-gas controller Cole Parmer (USA). The carbonization process took 2 h and the materials were then left to cool down to ambient temperature within the nitrogen atmosphere. The carbonized material was washed with a solution of HCl (0.15 M) and subsequently washed 5 times with 500 mL of hot distilled water and subsequently with room temperature distilled water until the pH of the rinse water remained constant between washing of the batches. The pH was measured with WTW Multi 3630 IDS with Sentix940 electrode. Finally, the materials were dried overnight at 105 °C, grounded and sieved to obtain particle size smaller than 0.25 mm.

A portion of the produced biochar material from both CH and CC was impregnated with ZnO nanoparticles using the precipitation method proposed by Wu et al. [36]. To impregnate, 10 g of biochar was mixed with 50 mL of NaOH solution (0.5 M) and the resulting suspension was heated to 60 °C while stirred constantly. When the suspension reached 60 °C, 50 mL of the zinc nitrate solution (0.5 M) was added to the suspension dropwise from the burette (in 30 min.). The temperature was then increased to 80 °C and maintained for 2 h to ensure that zinc hydroxide $Zn(OH)_2$ and ZnO nuclei precipitated from the solution. The suspension remained white in color for the rest of the synthesis, since on introduction of the zinc nitrate solution to the suspension white precipitate (zinc hydroxide $Zn(OH)_2$ and ZnO nuclei) was formed. The suspension was subsequently sonicated for 30 min in order to grow ZnO nanoparticles, filtered, and the residue was washed five times with 500 mL of room temperature distilled water. Finally, the materials

were dried in oven at 60 °C overnight and manually sieved to obtain particle size smaller than 0.25 mm. Prepared materials were designated: coffee husk biochar (CH-B), ZnO impregnated coffee husk biochar (CH-ZnO), corn cob biochar (CC-B) and ZnO impregnated corn cob biochar (CC-ZnO).

2.3. Characterization of adsorbents

The phase and crystallinity of adsorbents were studied by X-ray diffraction using Siemens D5000 diffractometer operated at 30 kV and 20 mA, CuKα (λ=1.5406 Å) radiation. The XRD patterns were collected in a 2Θ range from 10° to 80°. The interpretation of the XRD peaks was done using software Match¡3 (Crystal Impact, Germany). Nitrogen physisorption measurements at cryogenic conditions (-195.8 °C) were performed by the automated volumetric gas adsorption instruments ASAP 2020 and 2050 (Micromeritics, USA). To guarantee the accuracy of the obtained adsorption isotherms the high purity nitrogen (grade of 99.9995 vol.%) as well as helium (grade of 99.9995 vol.% used for determination of the free-space volume typically performed prior to analysis) were used. Before analysis, all materials were dried at 180 °C under a deep vacuum (< 1 Pa) for 24 h. The specific surface area, S_{BET}, was evaluated from the nitrogen adsorption isotherm in the range of relative pressure corresponding to p/p_0 = 0.05–0.25 using the standard Brunauer–Emmett–Teller (BET) procedure [37]. The mesopore surface area, S_{meso}, and the micropore volume, V_{micro}, were determined by the *t*-plot method [38]. The scanning electron microscope (SEM) Quanta FEG 450 (FEI, Czech Republic) was used for characterization of the morphology of the studied adsorbents. The Zn content was analyzed with X-ray fluorescence Niton XL3t 900 (XRF). The surface functional groups of the biochar were analyzed by a Fourier-transform infrared (FTIR) spectra analyzer (Thermo / Nicolet 360 FT-IR E.S.P. Spectrometer, USA). Raman spectra were recorded

using a Horiba (Japan) Jobin-Yvon LabRAM HR800 high-resolution confocal µ-Raman system with solid state laser (638 nm) excitation. The point of zero charge was determined by drift method using 10 mM KCl solution [3].

2.4. Equilibrium and kinetic experiments

Equilibrium and kinetic experiments were carried out to test the adsorption capacity of the materials. The equilibrium experiments were performed using eight different concentrations of As(V) and Pb(II): 2, 5, 15, 30, 40, 60, 80 and 100 mg/L, The volume of each solution was 50 mL and the adsorbent load was 4 g/L. The contact time was 48 h and the solutions were agitated in an orbital shaker New Brunswick Scientific, Innova 40 (UK). After contact time 10 mL aliquots were taken from each flask with different initial concentrations. Every aliquot was filtered through 0.45 µm filter and 50 µL of concentrated nitric acid was added to preserve them until the determination of As and Pb concentrations which was done using ICP-OES (Varian 720-ES, California, USA). The models of adsorption isotherm applied to the equilibrium data were Langmuir, Freundlich, Redlich-Peterson and Dubinnin-Raduskevich (see Table S1).

For the kinetic experiments, the adsorbent load was 3 g/L, the initial As(V) and Pb(II) concentration was 50 mg/L and the volume of the solution was 250 mL. Samples were agitated and aliquots were taken at each sampling time of 2, 5, 10, 20, 30, 60, 90, 120, 180 and 240 min respectively. Every taken aliquot was filtered through 0.45 µm filter and concentrated nitric acid (50 µL) was added to prevent precipitation of As or Pb until the ICP-OES analysis. The models of pseudo-first and pseudo-second order, Elovich and Intraparticle diffusion were applied to the kinetic data [39] (see Table S1).

The pH level (measured using WTW Multi 3630 IDS with Sentix940 electrode) at the beginning of the experiments was adjusted to 6.00 – 6.50 in every batch, for both

equilibrium and kinetic experiments. It was done in order to simulate pH of most of the natural water sources in north of Peru, also the ZnO works effectively [40] in pH range 5.8 - 6.8. To adjust pH NaOH and HCl solutions were used. In the case of equilibrium experiments, the initial (before addition of adsorbent) and final (after 48 h) pH levels were measured for every concentration; while in the case of kinetic experiments, pH levels were measured at different stages of the experiment.

The equilibrium adsorption uptakes of As(V) or Pb(II) on the adsorbents, q_e (mg/g) were calculated using the following equation:

$$q_e = \frac{(C_0 - C_e)V}{m_{BC}} \qquad (1)$$

where C_0 (mg/L) and C_e (mg/L) are initial concentration and the concentration of monitored element at equilibrium respectively. V (L) is the volume of the solution and m_{BC} (g) is the amount of biochar added.

The amount of As(V) or Pb(II) adsorbed at time t (q_t) was calculated using the following mass balance equation:

$$q_t = \frac{(C_0 - C_t)V}{m_{BC}} \qquad (2)$$

where C_0 is the initial concentration of As or Pb and C_t is the As or Pb concentration in solution at time t (mg/L). V is the total volume of solution (L) and m_{BC} is the mass of biochar (g) [39].

3. Results and discussion

3.1. Characterization of biochars

Textural properties of the prepared biochars are summarized in Table 1. It can be clearly seen that biochars prepared from corn cob had both higher specific surface area and the total pore volume compared to the biochars made from coffee husk. Material CH-B

reveals higher values of the total pore volume compared to CH-ZnO material. However, the deviation is due to the general heterogeneity of the parent biomass in terms of its microstructural properties rather than subsequent impregnation process as follows from the repeated measurements. On the other hand, it appears that impregnation process significantly improved the textural properties of CC material. Additionally, CH-B and CH-ZnO materials show values of the mesopore specific surface area as well as the volume of micropores below magnitudes accessible by the *t*-plot approach (the threshold limits are as follows: $S_{meso} < 1$ m^2/g, $V_{micro} < 1$ mm^3/g). The proportion of micropores over total pore volume is 29% for CC-B material and 26% for CC-ZnO material. Based on the comprehensive texture analysis, CC-ZnO material reveals the best properties in terms of microstructure.

Table 1 Textural characteristics of the produced adsorbents

Material	S_{BET} (m^2/g)	S_{meso} (m^2/g)	V_{tot} (mm$^3_{liq}$/g)	V_{micro} (mm$^3_{liq}$/g)
CH-B	4.6 ± 0.1	– (*)	7	– (*)
CH-ZnO	3.0 ± 0.2	– (*)	–	– (*)
CC-B	24.0 ± 1	14 ± 0.4	21	6
CC-ZnO	35.0 ± 1	15 ± 0.5	39	10

(*) below magnitudes accessible by the *t*-plot method ($S_{meso} < 1$ m^2/g, $V_{micro} < 1$ mm^3/g)

The crystal structure of prepared adsorbents was studied by XRD and the diffractograms (Figure 1a) of CH-B, CC-B and CH-ZnO showed amorphous character, the CC-ZnO showed combination of amorphous and crystalline structure. The wide diffraction peaks present at 12.2°, 23.6° and 43.2° were attributed to the amorphous phase of the biochar

[41] and these peaks were present in all the biochars (bare and ZnO impregnated). Diffraction peaks at 31.77°, 34.43°, 36.26°, 47.55°, 56.61° 62.87°, 66.39°, 67.96°, 69.10°, 72.58° and 76.98° were attributed to ZnO. The peaks correspond to (100), (002), (101), (102), (110), (103), (200), (112), (201), (004) and (202) planes, characteristic for wurtzite structure ZnO (COD ID 2300450, Match! Refpattern_96-230-0451) [20, 42, 43]. The crystalline ZnO was identified only in the CC-ZnO.

ATR-FTIR spectra of the materials were obtained to determine the presence of various functional groups on the biochars. Figure 1b reveals similar features, i.e. presence of similar functional groups on the surface of all four biochars. The peaks observed at 880 cm^{-1} can be attributed to aromatic C–H groups. The bands with the highest intensity located at 1100 cm^{-1} corresponds to C–O (hydroxyl functional group connected to the carbon atom) and/or ether group C–O–C. The intense band at 1560 cm^{-1} were due to C=C stretching in alkene. Finally, peaks at 1700 cm^{-1} can be ascribed to carbonyl group C=O. It follows that pyrolysis was carried out completely under inert atmosphere and most of oxygen-based compounds were eliminated since aforementioned bands show very low intensity.

The Raman spectra of biochar are shown in Figure 1c (it is a first – order Raman spectra, the excitation wavelength was λ_{exc} = 638 nm). The Raman spectra of biochar [44] [26] is similar to other carbonaceous materials like soot [45] or carbon molecular sieves [46]. The spectrum was de-convoluted with 5-band deconvolution model (G, D1, D2, D3, D4) [45] as shown in Figure 1d. G-band ("graphite") is caused by graphite lattice vibration mode with E2g symmetry and appears at ~1580 cm^{-1} [45, 47]. D-band ("disorder band" D1, D2, D3, D4) is caused by disorders (defects and in proximity of edges) in the graphene lattice [48, 49]. The D1 is the most prominent peak in disorder band and appears at ~1340 cm^{-1}. The I_{D1}/I_G band intensity gives information about degree of graphitisation

(decreasing of the I_{D1}/I_G indicates formation of graphitic structure) [45]. The de-convolution of the overlapping peaks suffers from great statistical uncertainty as demonstrated by [45]. The acquired I_{D1}/I_G values ranged from 0.9 to 1.1 (Table S2). The differences are not significant to be conclusive.

In order to determine the content of ZnO in the biochar materials the X-ray fluorescence (XRF) was used. The XRF determined the content of Zn (ppm) and it was converted to ZnO (wt.%). It was found out the biochars CH-B and CC-B both contained less than 0.01 % ZnO respectively. The ZnO impregnated CH-ZnO and CC-ZnO materials contained 0.48±0.00 % and 7.65±0.04 % respectively. The XRF results are in good agreement with the XRD diffractogram, where the crystalline ZnO was found only in the CC-ZnO. The detection minimum for XRD is 1 wt.% (for crystalline material) therefore according to the Figure 1a) the CH-ZnO diffractogram does not show ZnO phase because it is either below the detection minimum or the ZnO has amorphous structure.

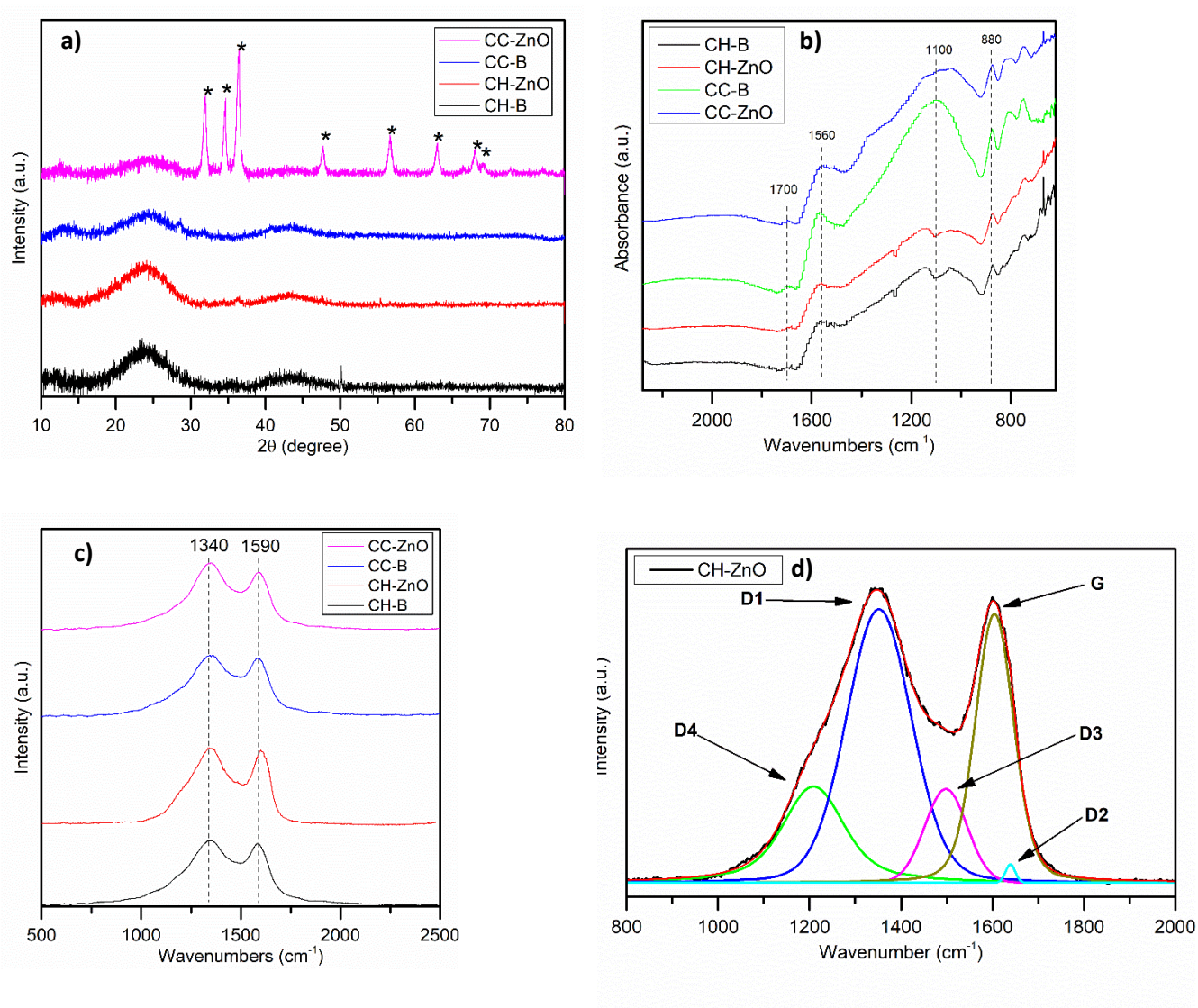

Figure 1. a) Diffractogram shows crystalline ZnO (marked with *), the biochar materials are amorphous. b) FTIR spectra with marked positions of various functional groups. c) The first-order spectra of biochars (CH-B, CH-ZnO, CC-B, CC-ZnO) exhibit two broad and strongly overlapping peaks with intensity maxima at ~1340 cm^{-1} and at ~1590 cm^{-1}. d) Curve fit with 5 band de-convolution for the first-order Raman spectra of CC-ZnO.

Surface morphology of the adsorbent plays a great role and the adsorption capacity greatly depends on the textural properties such as specific surface area and surface porosity. Figure 2 shows the SEM images of CH-B (a,b); CH-ZnO (c,d); CC-B (e,f); CC-ZnO (g,h);

and agglomerated ZnO is clearly observed on the surface of CC-ZnO biochar (Figure 2 g,h). Impregnated ZnO biochars show rugged surface hence increased surface area and porous channels.

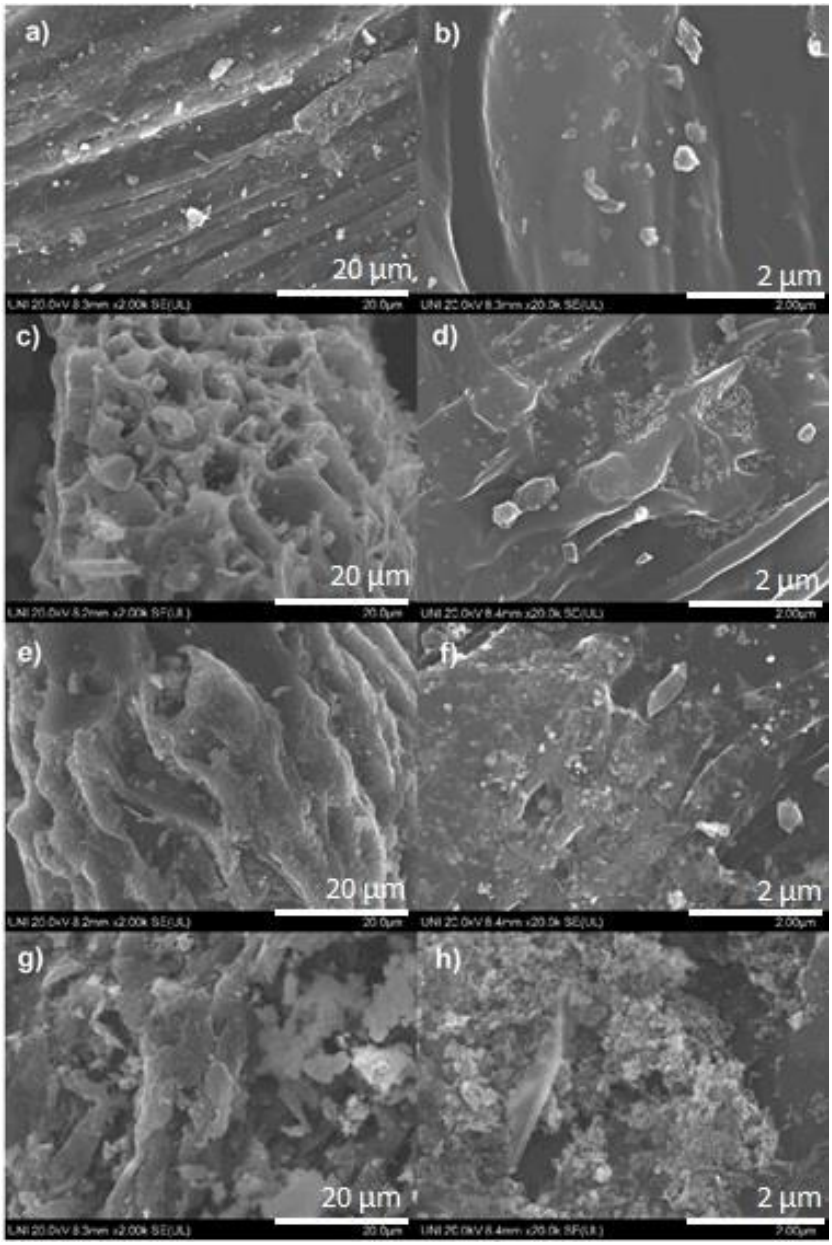

Figure 2. Morphology of the biochars, a, b) CH-B, c, d) CC-B, e, f) CH-ZnO, g, h) CC-ZnO.

The point of zero charge (PZC), for suspensions and colloids, determines conditions at which the net electrical charge on the surface of the dispersed particles is equal to zero.

The PZC is usually a pH value of the electrolyte (pH_{PZC}) at which the suspended particles of the analyte exhibit zero net electrical charge on their surface [39, 42]. The pH value at the point of zero charge (pH_{PZC}) was determined using the drift method (utilizing graphical analysis, Figure S1). The pH_{PZC} was 8.09±0.15 for CH-B, 7.84±0.15 for CH-ZnO, 8.13±0.15 for CC-B and 8.09±0.15 for CC-ZnO. In every case, pH values of the solution during equilibrium or kinetic adsorption experiments lower than pH_{PZC} make the surface of the adsorbent positive. In that sense, this situation favours, via electrostatic attraction [50], the adsorption of anions because of the attraction forces between the opposite charge of the adsorbent (positively charged) and adsorbate (negatively charged). Conversely, pH levels of the solution during equilibrium or kinetic adsorption experiments greater than pH_{PZC} make the surface of the adsorbent to be negatively charged. In that case, this situation favours the adsorption of cations because of the attraction forces between the opposite charge of the adsorbent (negatively charged) and adsorbate (positively charged).

3.2. Adsorption test with As(V) and Pb(II)

3.2.1. Adsorption Equilibrium

While Pb(II) was adsorbed by all of the four biochars, it was the CC-ZnO that showed the highest adsorption capacity. The C_e in solution was very low (one order lower) for CC-ZnO compared to other tested materials (Figure 3d). The Pb(II) maximum adsorption capacity of the CC-ZnO even surpassed the parameters of the test and the equilibrium concentration C_e was not determined. The ZnO impregnation improved adsorption of Pb(II) for both the materials and the improvement is best illustrated on comparison of Figure 3c and d. Compared to the bare materials the q_e increased one third for CH-ZnO and three times for CC-ZnO material. Although the equilibrium concentration was not

reached, in the case of CC-ZnO it can be said that it exceeded all other tested materials in Pb(II) adsorption test. Since the objective was the comparison of the biochars from different biomasses and biochars with and without ZnO, the initial load of adsorbents was kept the same for all the materials. For instance in the case of CC-ZnO it would be necessary to reduce the biochar load or increase the initial Pb(II) concentration in order to reach the equilibrium.

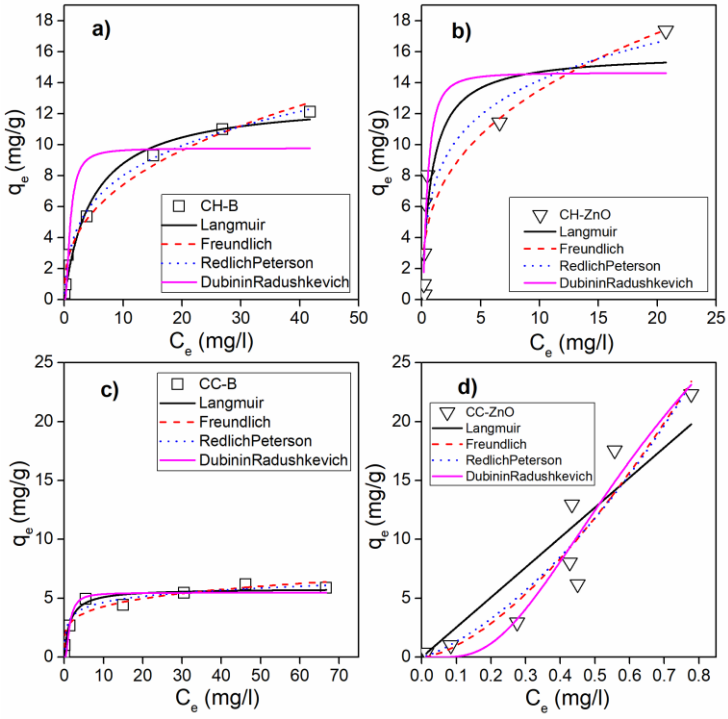

Figure 3. Pb(II) adsorption isotherms (30°C) by the produced materials.

Compared to Pb(II) adsorption all four biochars demonstrated lower values of q_e for As(V) adsorption. The CH-B showed very poor adsorption capacity of As(V) (less than 0.8 mg/g) and the randomness of the datapoints prevented use of adsorption models (Figure 4 a shows only datapoints). The ZnO impregnation also improved the adsorption of As(V), as evident from Figure 4. The CC-ZnO surpassed the rest of the materials and

showed one order lower C_e values. The adsorption capacity decreased in following order CC-ZnO > CH-ZnO > CC-B.

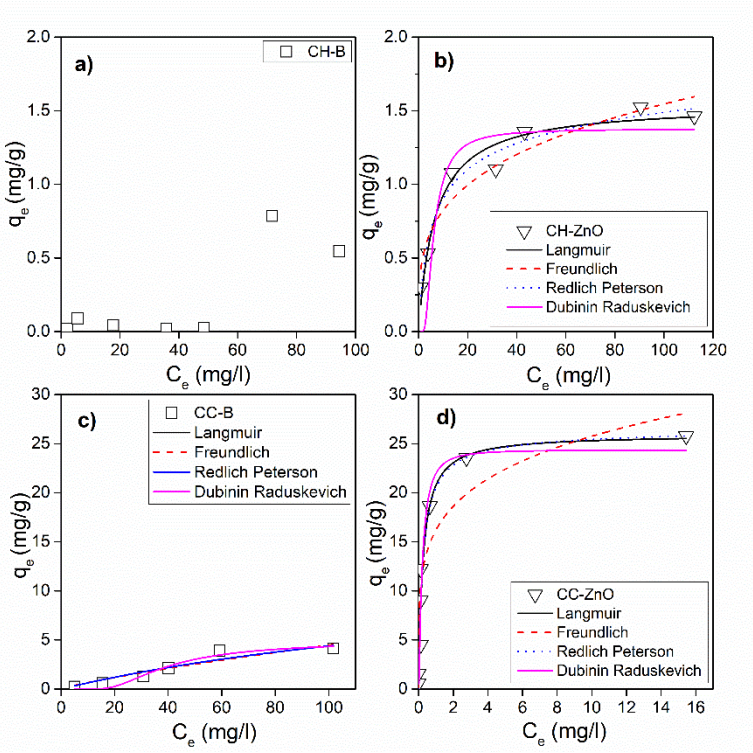

Figure 4. As(V) adsorption isotherms (30°C) by the produced materials.

From the comparison of coefficients of determination (R^2) and chi-square statistic (χ^2) (Table 2), the Pb(II) equilibrium test data of impregnated biochars fitted well with both Freundlich model and Dubinin-Radushkevich model. However, Dubinin-Radushkevich model provided the best fit and the Pb(II) maximum adsorption capacity q_e of the materials was determined from this model. In the case of CC-ZnO, the equilibrium was not reached, therefore the parameters calculated with the data are not final. The As(V) equilibrium test data was well fitted with Langmuir model and Redlich-Peterson model. The best fit was provided by the Langmuir model and the As(V) maximum adsorption capacity q_e from this model was used for comparison of the materials.

The separation factor R_L determined from the Langmuir model was found to be R_L <1 (the isotherm curve is favorable) for all of the tested materials in the Pb(II) adsorption. For the As(V) adsorption the R_L was R_L <1 for all tested materials with the exception of CH-B (R_L=1, which signifies the isotherm curve is linear).

Table 2. Parameters of the models applied to equilibrium test data.

		Pb					As				
		Q_0 (mg/g)	K_L (L/mg)		χ^2	R^2	Q_0 (mg/g)	K_L (L/mg)		χ^2	R^2
Langmuir	**CH-B**	12.958	0.211		0.600	0.979	- (*)	-		-	-
	CH-ZnO	15.911 (**)	1.212		7.315	0.837	1.545	0.148		0.011	0.960
	CC-B	5.829	0.696		0.316	0.945	13.058	0.005		0.307	0.910
	CC-ZnO	94368.477 (**)	0.000		12.498	0.833	25.936	3.996		6.254	0.944
		K_F (mg/g)/(mg/L)^n	**n**		χ^2	R^2	K_F (mg/g)/(mg/L)^n	**n**		χ^2	R^2
Freundlich	**CH-B**	3.115	0.377		0.425	0.985	- (*)	-		-	-
	CH-ZnO	6.081 (**)	0.347		6.845	0.848	0.438	0.274		0.019	0.929
	CC-B	2.664	0.209		0.360	0.938	0.100	0.827		0.364	0.894
	CC-ZnO	34.520 (**)	1.544		7.643	0.898	16.186	0.202		13.360	0.880
		K_{RP} (L/g)	a_{RP} (mg/L)	**g**	χ^2	R^2	K_{RP} (L/g)	a_{RP} (mg/L)	**g**	χ^2	R^2
Redlech-Peterson	**CH-B**	9.217	1.907	0.741	0.153	0.996	- (*)	-	-	-	-
	CH-ZnO	31.220 (**)	3.348	0.799	7.805	0.861	0.362	0.390	0.889	0.010	0.970
	CC-B	15.223	4.279	0.870	0.276	0.960	0.066	0.005	1.000	0.410	0.910
	CC-ZnO	0.389 (**)	-0.989	0.008	9.555	0.894	108.319	4.291	0.987	7.468	0.944
		q_{DR} (mg/g)	k_{DR} (mol^2/kJ^2)		χ^2	R^2	q_{DR}	k_{DR}		χ^2	R^2
Dubinin-Radushkevich	**CH-B**	9.769	0.235		4.369	0.844	- (*)	-		-	-
	CH-ZnO	14.642 (**)	0.084		6.988	0.845	1.376	5.197		0.015	0.732
	CC-B	5.476	0.379		0.486	0.916	4.885	193.235		0.167	0.951
	CC-ZnO	51.784 (**)	0.186		6.496	0.913	24.363	0.034		7.205	0.935

(*) Data not reported because of very low values and randomness of the datapoints

(**) The equilibrium was not reached
The initial (before addition of adsorbent) and final (after 48 h) pH levels were measured for every concentration and showed in the table S4.

The Freundlich intensity parameter n was found to be n <1 (the isotherm curve is favorable) with the exception of CC-ZnO (n > 1, which signifies the isotherm curve is linear) for the Pb(II) adsorption. In As(V) adsorption the n was found to be n <1.

The magnitude of energy E (kJ/mol) determined from Dubinin-Radushkevich model (see Table S3) indicated that, for both toxic elements, the adsorption energies of the experiments with biochars impregnated with ZnO were higher than those for bare biochars. According to literature the magnitude of E is related to the type of mechanism that takes place during the adsorption: physical (E<20 kJ/mol), ion exchange (E= 8 – 16 kJ/mol) or chemical (E= 20 – 200 kJ/mol) [39, 51-54]. The energies E determined for all experiments (ranged from 0.028 kJ/mol to 3.820 kJ/mol) were within the physical adsorption (<20 kJ/mol). However, comparing bare and impregnated materials, it is evident that in the case of impregnated materials an additional mechanism could be involved, and it might be ion exchange.

3.2.2. Adsorption Kinetic

It can be noticed from figures 5 and 6 that the impregnation with ZnO improved the Pb(II) and As(V) adsorption rate and equilibrium adsorption of the biochars made from both residual agrowaste biomasses. In Pb(II) kinetic adsorption test the ZnO impregnated materials showed significantly improved adsorption capacity and reached the equilibrium sooner. The sorption capacity q_t for ZnO impregnated biochars was four times resp. two times bigger for CH-ZnO resp. CC-ZnO compared to bare biochars CH resp. CC (Figure 5). Similar results were achieved in the As(V) kinetic adsorption test. The sorption capacity q_t for ZnO impregnated biochars was two times resp. five times bigger for CH-

ZnO resp. CC-ZnO compared to bare biochars CH resp. CC (Figure 6). In both kinetic tests the adsorbate showed great affinity to CC-ZnO.

From the comparison of coefficients of determination (R^2) and chi-square statistic (χ^2), the Pb(II) kinetic test data (Table 3) were best fitted with Elovich model (R^2 = 0.975-0.984 and χ^2 = 0.032-0.712), the As(V) kinetic test data was also best fitted with Elovich model. However, the PSO model described the kinetic data good as well. From the Elovich model, is evident that comparison of *a* (the initial adsorption rate in mg/(g.min)) for Pb(II) and As(V), the biochar materials impregnated with ZnO presented higher initial adsorption rate than the bare biochars (For Pb(II) in the following order CC-ZnO>CH-ZnO>CH-B>CC-B; while for As(V) it was CC-ZnO>CC-B>CH-ZnO>CH-B). If we consider q_e (equilibrium adsorption capacity in mg/g), calculated by PSO model, it is evident that biochars with ZnO impregnation show higher equilibrium adsorption capacity than the bare biochars (For Pb(II) in the following order CC-ZnO>CH-ZnO>CC-B>CH-B; while for As(V) it was CC-ZnO>CH-ZnO>CH-B>CC-B).

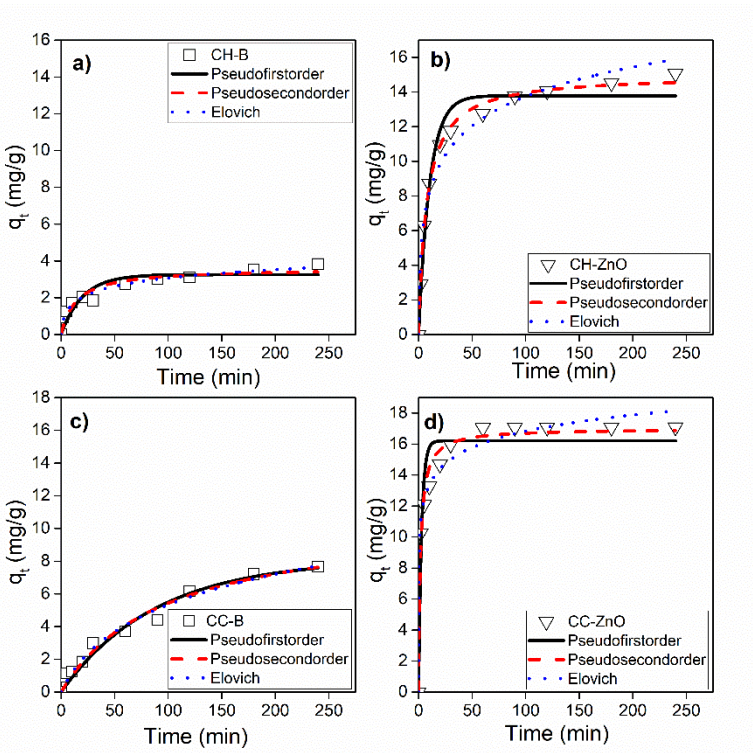

Figure 5. Pb(II) kinetic data by the produced materials.

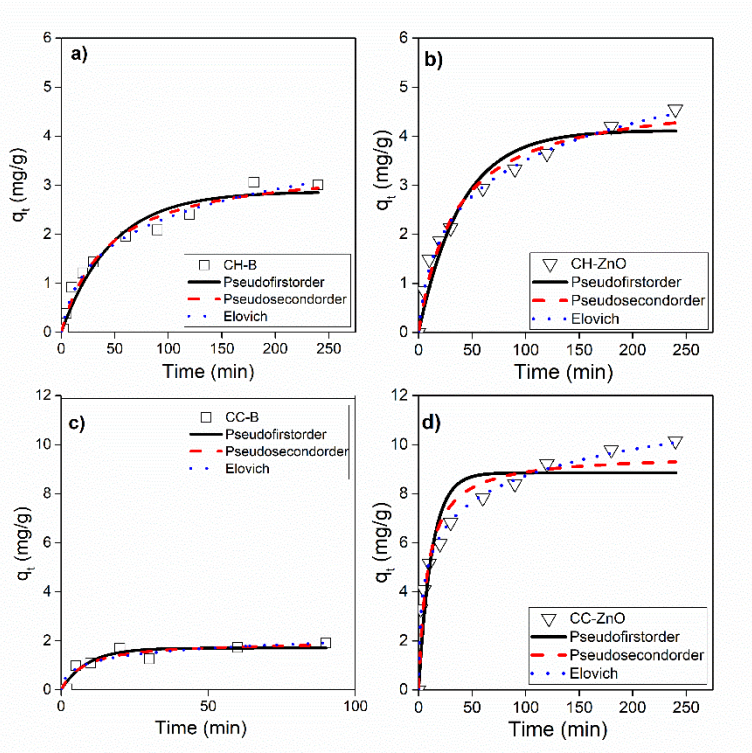

Figure 6. As(V) kinetic data by the produced materials.

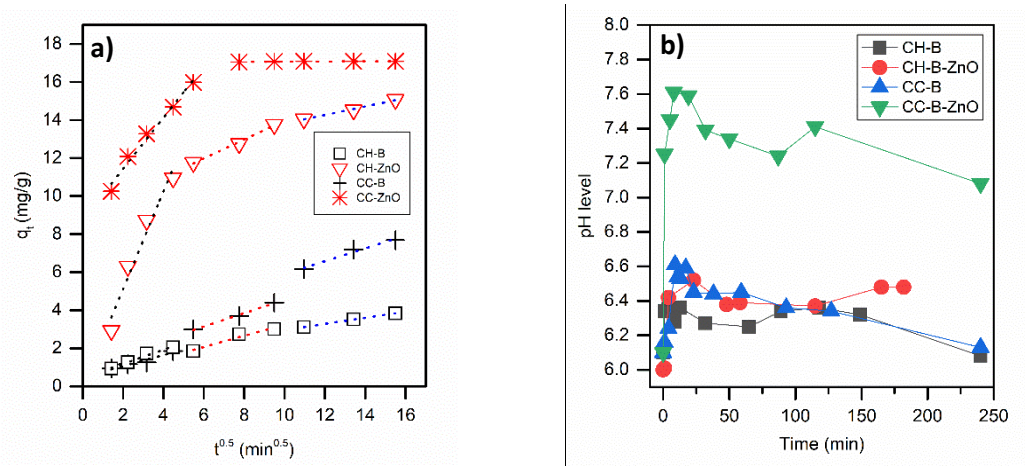

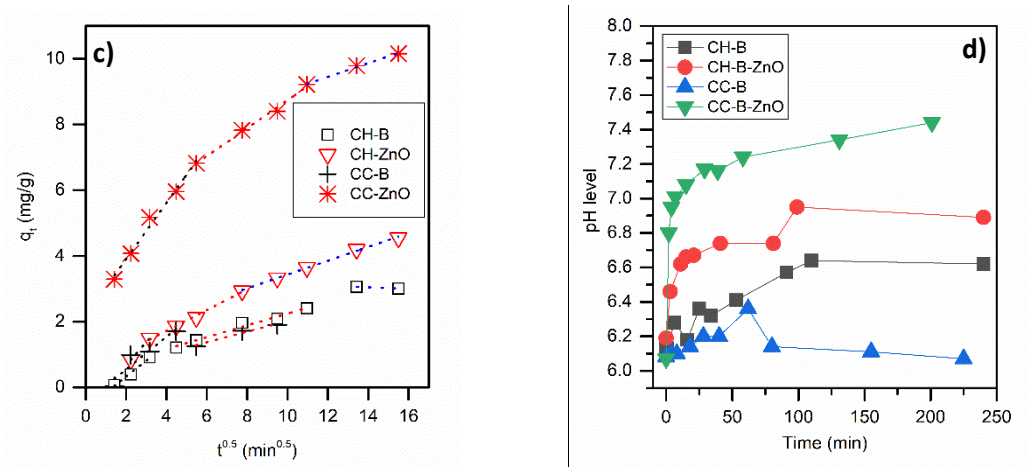

Figure 7. Intraparticle diffusion model of Pb(II) (a) and As(V) (c). pH behavior during the Pb (b) and As (d) kinetic tests

Table 3. Parameters of the models applied to Kinetic test data.

		Pb				As			
		q_e (mg/g)	k_1 (min^{-1})	χ^2	R^2	q_e (mg/g)	k_1 (min^{-1})	χ^2	R^2
PFO	**CH-B**	3.249	0.050	0.213	0.862	2.867	0.021	0.054	0.960
	CH-ZnO	13.785	0.097	0.768	0.973	4.117	0.025	0.125	0.950
	CC-B	8.108	0.011	0.270	0.966	1.703	0.113	0.064	0.898
	CC-ZnO	16.208	0.360	2.013	0.932	8.847	0.081	1.321	0.878
		q_e (mg/g)	k_2 (g/mg.min)	χ^2	R^2	q_e (mg/g)	k_2 (g/mg.min)	χ^2	R^2
PSO	**CH-B**	3.604	0.020	0.113	0.927	3.459	0.007	0.028	0.979
	CH-ZnO	15.004	0.009	0.097	0.997	4.878	0.006	0.051	0.979
	CC-B	10.753	0.001	0.225	0.972	1.989	0.062	0.061	0.903
	CC-ZnO	16.995	0.034	0.516	0.983	9.622	0.012	0.571	0.947
		a (mg/g.min)	b (mg/g)	χ^2	R^2	a (mg/g.min)	b (mg/g)	χ^2	R^2
Elovich	**CH-B**	0.698	1.523	0.032	0.979	0.122	1.160	0.017	0.988
	CH-ZnO	6.563	0.407	0.712	0.975	0.243	0.890	0.009	0.996
	CC-B	0.140	0.319	0.184	0.977	0.660	2.652	0.004	0.973
	CC-ZnO	1065.901	0.664	0.468	0.984	4.279	0.644	0.040	0.996
		K_p	C	χ^2	R^2	K_p	C	χ^2	R^2

		(mg/g.min$^{0.5}$)	(mg/g)			(mg/g.min$^{0.5}$)	(mg/g)		
	CH-B	0.222	0.688	0.109	0.929	0.222	0.688	0.109	0.929
Intraparticle	**CH-ZnO**	0.869	4.247	6.309	0.776	0.869	4.247	6.309	0.776
model	**CC-B**	0.519	-0.090	0.126	0.984	0.519	-0.090	0.126	0.984
	CC-ZnO	0.741	8.813	13.562	0.540	0.741	8.813	13.562	0.540

From the intraparticle diffusion model (Figure 7 a, c) and Table 3) it is apparent that there is presence of multiple linear regions. The intraparticle diffusion is therefore not the sole mechanism of Pb(II) and As(V) adsorption and the adsorption process consists of multiple mechanisms [39]

3.3. Effect of ZnO load

The impregnation with ZnO proved to be beneficial to both precursors (coffee husk and corn cob). The presence of ZnO in significant amount was detected by XRF only in CH-ZnO and CC-ZnO. In CC-ZnO it was also confirmed from XRD diffractogram. The ZnO in CH-ZnO was not detected by XRD because it is below 1 wt.% (of crystalline material) detection minimum. The relatively low ZnO content in CH-ZnO biochar suggests limited success of impregnation process in the case of CH precursor.

In equilibrium adsorption test with Pb(II) and kinetic adsorption test with As(V) the CH biochar showed higher adsorption capacity compared to CC biochar. We can surmise that the CH-ZnO could rival adsorption properties of CC-ZnO if the impregnation loading was same for both materials. Therefore, the ZnO impregnation of CH biochar could benefit from further study.

In the case of biochars made of corncob, the impregnation with ZnO improved its textural properties in terms of microporosity. This tendency was not the same for the biochar made of coffee husk. The SEM images of CC-ZnO show presence of ultrafine particle aggregates (which can be reasonable to presume are ZnO) on the surface of CC biochar

particles. The presence of ultrafine particle agglomerates could be very well responsible for the improvement of the textural properties of the material CC-ZnO in terms of microstructure mainly.

Bare biochar made of corncob showed better textural properties than bare biochar made of coffee husk CH-B. In that sense in our previous study [2], we found that corncob as raw material showed better textural properties than coffee husk and makes adsorbents with better textural properties as well. This study is in accordance with the previous finding. The better textural properties in the material CC-B allow the precursor of ZnO (zinc nitrate tetrahydrate) to penetrate better during the impregnation process compare to CH-B, thus obtain higher ZnO concentration loaded in the CC-ZnO surface. This could be one of the reason for better results in the case of CC-ZnO, however, further studies need to be done to obtain information related to how the ZnO loads to the biochar surface in order to understand better why in CC-B, the ZnO was successful loaded.

All the kinetic and equilibrium adsorption tests for both pollutants showed improved adsorption of ZnO impregnated biochars. The ZnO impregnated biochar showed higher adsorption capacity for the model pollutants and increased affinity of pollutant to the adsorbent. Although the equilibrium was not achieved with most of the materials, the main goal of comparison of two different biochars from residual biomass precursors (coffee husk and corn cob) and their ZnO impregnated forms was accomplished and clear conclusions can be drawn.

In a water solution with pH of 8 (near the pH_{pzc} of our materials) and Eh around 0 V, the As(V) ions have a negative (as oxyanion) or neutral charge [55] and Pb(II) ions have a positive charge [56]. The pH during the kinetic tests (figures 7 b and d) was below the pH_{pzc} (Figure S2) for all the experiments, which suggests only adsorption of anions should have been favored e.g. only of As(V) oxyanions. But the improvement in adsorption after

ZnO impregnation was seen for both As(V) and Pb(II). This fact can be explained by presence of active sites for adsorption of metals ions on ZnO thanks to its porous structure and surface and presence of functional groups due to positively charged Zn ions and negatively charged O ions [14, 19].

In the case of Pb(II) adsorption (Figure 7b), pH for all the materials increased rapidly in the first stage (10 -15 min) of the experiments because of addition and dispersion of the adsorbent material. After the first stage, pH in most of the cases decreased with a varying speed. This decrease in pH can be explained by ionic exchange between adsorbent (both bare biochars and ZnO impregnated biochars) and Pb(II) ions. In the case of ZnO, various authors [14, 16] conclude that Pb(II) binds to the surface hydroxyl groups of ZnO and release protons to the solution. The release of the protons causes the decrease of pH after adsorbent addition. In the case of bare biochars, the ion exchange can occur with the oxygenated functional groups located on surface, with the release of protons as well.

In the case of As(V) adsorption (Figure 7 d), pH for all the experiments increased rapidly in the first stage because of the addition and dispersion of the adsorbent material and then the pH had a small tendency to increase in most cases, but the CC-B. For the material CC-B the pH level increased when the material is added, spiked around 60 min. time and then the pH decreased slightly and kept constant. This is in correlation with the low As(V) adsorption of that material. Adsorption between negatively charged oxyanions As(V) and ZnO, might occur through ligand exchange of the hydroxyl group from Zn-OH to form Zn-O-As complex [17].

4. Conclusion

Coffee husk and corn cob based biochars were produced in mild conditions 600 °C/2 h and then impregnated with ZnO. The effect of this modification on adsorption of Pb(II)

and As(V) was tested in aqueous solutions. Both biochars and their ZnO impregnated biochars removed Pb(V) and As(II) from aqueous solutions. The adsorption properties of both natural materials were improved with the ZnO impregnation and the adsorption capacities for Pb(II) and As(V) were several times increased. ZnO impregnation improved the microstructure of the biochar based on corncob and increase the active sites to improve adsorption of both toxic elements. Based on the both equilibrium and kinetic results it was clear that corncob derived biochar with ZnO impregnation outperformed the rest and can be considered as a promising material for use in water treatment.

Acknowledgement

The authors would like to thank Newton Paulet Found E009 - Contract 002-FONDECYT (CONCYTEC). The work was supported from ERDF "Institute of Environmental Technology – Excellent Research " (No. CZ.02.1.01/0.0/0.0/16_019/0000853) and by the ESF in „Science without borders“ project, reg. nr. CZ.02.2.69/0.0./0.0./16_027/0008463 within the Operational Programme Research, Development and Education. The authors would also like to thank Jana Kalbáčová who provided valuable insight in Raman spectra modeling. Universidad Nacional de Tumbes supported also this research (CANON Project - Resolution 180-2016/UNT-R). The University of Salford is acknowledged for the ICP-OES analysis in this study.

References

[1] MINAGRI, Valor Bruto de la Producción Agropecuaria - Peru. 2019, Ministery of Agriculture and Drainage, Peru, 2018.
[2] G.J.F. Cruz, L. Matějová, M. Pirilä, K. Ainassaari, C.A. Canepa, J. Solis, J.F. Cruz, O. Šolcová, R.L. Keiski, A Comparative Study on Activated Carbons Derived from a Broad Range of Agro-industrial Wastes in Removal of Large-Molecular-Size Organic Pollutants in Aqueous Phase, Water, Air, & Soil Pollution 226 (2015).

[3] G.J.F. Cruz, L. Kuboňová, D.Y. Aguirre, L. Matějová, P. Peikertová, I. Troppová, E. Cegmed, A. Wach, P. Kustrowski, M.M. Gomez, L. Obalová, Activated Carbons Prepared from a Broad Range of Residual Agricultural Biomasses Tested for Xylene Abatement in the Gas Phase, ACS Sustainable Chemistry & Engineering 5 (2017) 2368-2374.
[4] S. Wang, H. Nam, H. Nam, Preparation of activated carbon from peanut shell with KOH activation and its application for H2S adsorption in confined space, Journal of Environmental Chemical Engineering 8 (2020) 103683.
[5] M.H. Park, S. Jeong, J.Y. Kim, Adsorption of NH3-N onto rice straw-derived biochar, Journal of Environmental Chemical Engineering 7 (2019) 103039.
[6] Z. Mahdi, A. El Hanandeh, Q.J. Yu, Preparation, characterization and application of surface modified biochar from date seed for improved lead, copper, and nickel removal from aqueous solutions, Journal of Environmental Chemical Engineering 7 (2019) 103379.
[7] H.S. Kambo, A. Dutta, A comparative review of biochar and hydrochar in terms of production, physico-chemical properties and applications, Renewable and Sustainable Energy Reviews 45 (2015) 359-378.
[8] Z. Zhou, Y.-g. Liu, S.-b. Liu, H.-y. Liu, G.-m. Zeng, X.-f. Tan, C.-p. Yang, Y. Ding, Z.-l. Yan, X.-x. Cai, Sorption performance and mechanisms of arsenic(V) removal by magnetic gelatin-modified biochar, Chemical Engineering Journal 314 (2017) 223-231.
[9] A. Bhatnagar, W. Hogland, M. Marques, M. Sillanpää, An overview of the modification methods of activated carbon for its water treatment applications, Chemical Engineering Journal 219 (2013) 499-511.
[10] M. Azizi-Lalabadi, A. Ehsani, B. Ghanbarzadeh, B. Divband, Polyvinyl alcohol/gelatin nanocomposite containing ZnO, TiO2 or ZnO/TiO2 nanoparticles doped on 4A zeolite: Microbial and sensory qualities of packaged white shrimp during refrigeration, International Journal of Food Microbiology 312 (2020) 108375.
[11] R. Saravanan, V.K. Gupta, V. Narayanan, A. Stephen, Comparative study on photocatalytic activity of ZnO prepared by different methods, Journal of Molecular Liquids 181 (2013) 133-141.
[12] N. Kataria, V.K. Garg, Optimization of Pb (II) and Cd (II) adsorption onto ZnO nanoflowers using central composite design: isotherms and kinetics modelling, Journal of Molecular Liquids 271 (2018) 228-239.
[13] X. Hu, Y. Qiao, B. Wang, Y. Hou, F. Zheng, Q. Li, Efficient Pb2+ adsorption of biomorphic porous ZnO derived from legume straw, Environmental Progress & Sustainable Energy 38 (2019).
[14] M.Y. Haddad, H.F. Alharbi, Enhancement of heavy metal ion adsorption using electrospun polyacrylonitrile nanofibers loaded with ZnO nanoparticles, Journal of Applied Polymer Science 136 (2019).
[15] S. Xu, X. Jiang, L. Liu, Z. Wang, X. Zhang, Y. Peng, M. Cao, Preparation of PVA/tetra-ZnO composite with framework-supported pore-channel structure and the removal research of lead ions, Environ Sci Pollut Res Int 26 (2019) 24062-24074.
[16] Y. Kikuchi, Q. Qian, M. Machida, H. Tatsumoto, Effect of ZnO loading to activated carbon on Pb(II) adsorption from aqueous solution, Carbon 44 (2006) 195-202.
[17] R. Li, J.J. Wang, L.A. Gaston, B. Zhou, M. Li, R. Xiao, Q. Wang, Z. Zhang, H. Huang, W. Liang, H. Huang, X. Zhang, An overview of carbothermal synthesis of metal–biochar composites for the removal of oxyanion contaminants from aqueous solution, Carbon 129 (2018) 674-687.
[18] A.S. Ibupoto, U.A. Qureshi, M. Arain, F. Ahmed, Z. Khatri, R.Z. Brohi, I.S. Kim, Z. Ibupoto, Zno/Carbon nanofibers for efficient adsorption of lead from aqueous solutions, Environ Technol (2019) 1-11.
[19] S. Singh, K.C. Barick, D. Bahadur, Functional Oxide Nanomaterials and Nanocomposites for the Removal of Heavy Metals and Dyes, Nanomaterials and Nanotechnology 3 (2013) 3-20.
[20] E.A. Dil, M. Ghaedi, A. Ghaedi, A. Asfaram, M. Jamshidi, M.K. Purkait, Application of artificial neural network and response surface methodology for the removal of crystal violet by

zinc oxide nanorods loaded on activate carbon: kinetics and equilibrium study, Journal of the Taiwan Institute of Chemical Engineers 59 (2016) 210-220.
[21] M. Ghaedi, A. Ansari, M.H. Habibi, A.R. Asghari, Removal of malachite green from aqueous solution by zinc oxide nanoparticle loaded on activated carbon: Kinetics and isotherm study, Journal of Industrial and Engineering Chemistry 20 (2014) 17-28.
[22] H. Nourmoradi, A.R. Ghiasvand, Z. Noorimotlagh, Removal of methylene blue and acid orange 7 from aqueous solutions by activated carbon coated with zinc oxide (ZnO) nanoparticles: equilibrium, kinetic, and thermodynamic study, Desalination and Water Treatment 55 (2014) 252-262.
[23] P. Raizada, P. Singh, A. Kumar, G. Sharma, B. Pare, S.B. Jonnalagadda, P. Thakur, Solar photocatalytic activity of nano-ZnO supported on activated carbon or brick grain particles: Role of adsorption in dye degradation, Applied Catalysis A: General 486 (2014) 159-169.
[24] G.J.F. Cruz, M.M. Gomez, J.L. Solis, J. Rimaycuna, R.L. Solis, J.F. Cruz, B. Rathnayake, R.L. Keiski, Composites of ZnO nanoparticles and biomass based activated carbon: adsorption, photocatalytic and antibacterial capacities, Water Sci Technol 2017 (2018) 492-508.
[25] S. Wang, Y. Zhou, S. Han, N. Wang, W. Yin, X. Yin, B. Gao, X. Wang, J. Wang, Carboxymethyl cellulose stabilized ZnO/biochar nanocomposites: Enhanced adsorption and inhibited photocatalytic degradation of methylene blue, Chemosphere 197 (2018) 20-25.
[26] M. Chen, C. Bao, D. Hu, X. Jin, Q. Huang, Facile and low-cost fabrication of ZnO/biochar nanocomposites from jute fibers for efficient and stable photodegradation of methylene blue dye, Journal of Analytical and Applied Pyrolysis 139 (2019) 319-332.
[27] P. Gholami, L. Dinpazhoh, A. Khataee, Y. Orooji, Sonocatalytic activity of biochar-supported ZnO nanorods in degradation of gemifloxacin: Synergy study, effect of parameters and phytotoxicity evaluation, Ultrason Sonochem 55 (2019) 44-56.
[28] C. Li, L. Zhang, Y. Gao, A. Li, Facile synthesis of nano ZnO/ZnS modified biochar by directly pyrolyzing of zinc contaminated corn stover for Pb(II), Cu(II) and Cr(VI) removals, Waste Manag 79 (2018) 625-637.
[29] J. Yu, C. Jiang, Q. Guan, P. Ning, J. Gu, Q. Chen, J. Zhang, R. Miao, Enhanced removal of Cr(VI) from aqueous solution by supported ZnO nanoparticles on biochar derived from waste water hyacinth, Chemosphere 195 (2018) 632-640.
[30] B.G. Marshall, M.M. Veiga, R.J. Kaplan, R. Adler Miserendino, G. Schudel, B.A. Bergquist, J.R.D. Guimaraes, L.G.S. Sobral, C. Gonzalez-Mueller, Evidence of transboundary mercury and other pollutants in the Puyango-Tumbes River basin, Ecuador-Peru, Environ Sci Process Impacts 20 (2018) 632-641.
[31] D. Mondal, R. Periche, B. Tineo, L.A. Bermejo, M.M. Rahman, A.B. Siddique, M.A. Rahman, J.L. Solis, G.J.F. Cruz, Arsenic in Peruvian rice cultivated in the major rice growing region of Tumbes river basin, Chemosphere (2019) 125070.
[32] D. Mondal, D.A. Polya, Rice is a major exposure route for arsenic in Chakdaha block, Nadia district, West Bengal, India: A probabilistic risk assessment, Applied Geochemistry 23 (2008) 2987-2998.
[33] A.A. Meharg, F.-J. Zhao, Risk from arsenic in rice grain, Arsenic & Rice, Springer2012, pp. 31-50.
[34] G.J. Norton, P.N. Williams, E.E. Adomako, A.H. Price, Y. Zhu, F.-J. Zhao, S. McGrath, C.M. Deacon, A. Villada, A. Sommella, Lead in rice: Analysis of baseline lead levels in market and field collected rice grains, Science of the total environment 485 (2014) 428-434.
[35] Y. Fakhri, G. Bjørklund, A.M. Bandpei, S. Chirumbolo, H. Keramati, R.H. Pouya, A. Asadi, N. Amanidaz, M. Sarafraz, A. Sheikhmohammad, Concentrations of arsenic and lead in rice (Oryza sativa L.) in Iran: a systematic review and carcinogenic risk assessment, Food and chemical toxicology 113 (2018) 267-277.
[36] C. Wu, X. Qiao, J. Chen, H. Wang, F. Tan, S. Li, A novel chemical route to prepare ZnO nanoparticles, Materials Letters 60 (2006) 1828-1832.

[37] S. Brunauer, P.H. Emmett, E. Teller, Adsorption of gases in multimolecular layers, Journal of the American chemical society 60 (1938) 309-319.
[38] J. De Boer, B. Lippens, B. Linsen, J. Broekhoff, A. Van den Heuvel, T.J. Osinga, Thet-curve of multimolecular N2-adsorption, Journal of Colloid and Interface Science 21 (1966) 405-414.
[39] H.N. Tran, S.J. You, A. Hosseini-Bandegharaei, H.P. Chao, Mistakes and inconsistencies regarding adsorption of contaminants from aqueous solutions: A critical review, Water Res 120 (2017) 88-116.
[40] S. Lata, S.R. Samadder, Removal of arsenic from water using nano adsorbents and challenges: A review, J Environ Manage 166 (2016) 387-406.
[41] M. Zbair, Z. Anfar, H. Ait Ahsaine, N. El Alem, M. Ezahri, Acridine orange adsorption by zinc oxide/almond shell activated carbon composite: Operational factors, mechanism and performance optimization using central composite design and surface modeling, J Environ Manage 206 (2018) 383-397.
[42] M. Sharma, M. Joshi, S. Nigam, S. Shree, D.K. Avasthi, R. Adelung, S.K. Srivastava, Y. Kumar Mishra, ZnO tetrapods and activated carbon based hybrid composite: Adsorbents for enhanced decontamination of hexavalent chromium from aqueous solution, Chemical Engineering Journal 358 (2019) 540-551.
[43] M. Ghaedi, M.N. Biyareh, S.N. Kokhdan, S. Shamsaldini, R. Sahraei, A. Daneshfar, S. Shahriyar, Comparison of the efficiency of palladium and silver nanoparticles loaded on activated carbon and zinc oxide nanorods loaded on activated carbon as new adsorbents for removal of Congo red from aqueous solution: Kinetic and isotherm study, Materials Science and Engineering: C 32 (2012) 725-734.
[44] M. Li, H. Zhang, T. Xiao, S. Wang, B. Zhang, D. Chen, M. Su, J. Tang, Low-cost biochar derived from corncob as oxygen reduction catalyst in air cathode microbial fuel cells, Electrochimica Acta 283 (2018) 780-788.
[45] A. Sadezky, H. Muckenhuber, H. Grothe, R. Niessner, U. Pöschl, Raman microspectroscopy of soot and related carbonaceous materials: Spectral analysis and structural information, Carbon 43 (2005) 1731-1742.
[46] C. Sisu, R. Iordanescu, V. Stanciu, I. Stefanescu, A.M. Vlaicu, V.V. Grecu, RAMAN SPECTROSCOPY STUDIES OF SOME CARBON MOLECULAR SIEVES, Digest Journal of Nanomaterials and Biostructures 11 (2016) 435-442.
[47] S. Reich, C. Thomsen, Raman spectroscopy of graphite, Philosophical Transactions of the Royal Society London A 362 (2004) 2271–2288.
[48] A.C. Ferrari, D.M. Basko, Raman spectroscopy as a versatile tool for studying the properties of graphene, Nat Nanotechnol 8 (2013) 235-246.
[49] S.S. Nanda, M.J. Kim, K.S. Yeom, S.S.A. An, H. Ju, D.K. Yi, Raman spectrum of graphene with its versatile future perspectives, TrAC Trends in Analytical Chemistry 80 (2016) 125-131.
[50] G. Vyavahare, P. Jadhav, J. Jadhav, R. Patil, C. Aware, D. Patil, A. Gophane, Y.-H. Yang, R. Gurav, Strategies for crystal violet dye sorption on biochar derived from mango leaves and evaluation of residual dye toxicity, Journal of Cleaner Production 207 (2019) 296-305.
[51] A.U. Itodo, H.U. Itodo, Sorption Energies Estimation Using Dubinin-Radushkevich and Temkin Adsorption Isotherms, Life Science Journal 7 (2010) 31-39.
[52] K. Vijayaraghavan, T.V. Padmesh, K. Palanivelu, M. Velan, Biosorption of nickel(II) ions onto Sargassum wightii: application of two-parameter and three-parameter isotherm models, J Hazard Mater 133 (2006) 304-308.
[53] P. Senthil Kumar, C. Senthamarai, A. Durgadevi, Adsorption kinetics, mechanism, isotherm, and thermodynamic analysis of copper ions onto the surface modified agricultural waste, Environmental Progress & Sustainable Energy 33 (2014) 28-37.
[54] F. Helfferich, Ion exchange, New York: McGraw- Hill Book.1962.
[55] P. Lu, C. Zhu, Arsenic Eh–pH diagrams at 25°C and 1 bar, Environmental Earth Sciences 62 (2010) 1673-1683.

[56] P.A. Nikolaychuk, The revised potential – pH diagram for Pb – H2O system, Ovidius University Annals of Chemistry 29 (2018) 55-67.

Figure Captions

Figure 1. a) Diffractogram shows crystalline ZnO (marked with *), the biochar materials are amorphous. b) The first-order spectra of biochars (CH-B, CH-ZnO, CC-B, CC-ZnO) exhibit two broad and strongly overlapping peaks with intensity maxima at ~1340 cm^{-1} and at ~1590 cm^{-1}. c) Curve fit with 5 band de-convolution for the first-order Raman spectra of CC-ZnO. d) The main Raman bands for excitation frequency 638 nm.

Figure 2. Morphology of the biochars, a, b) CH-B, c, d) CC-B, e, f) CH-ZnO, g, h) CC-ZnO.

Figure 3. Pb(II) adsorption isotherms (30°C) by the produced materials.

Figure 4. As(V) adsorption isotherms (30°C) by the produced materials.

Figure 5. Pb(II) kinetic data by the produced materials (a-d).

Figure 6. As(V) kinetic data by the produced materials.

Figure 7. Intraparticle diffusion model of Pb(II) (a) and As(V) (c). pH behavior during the Pb (b) and As (d) kinetic tests

Tables and Figures

Table 1 Textural characteristics of the produced adsorbents

Material	S_{BET} **(m^2/g)**	S_{meso} **(m^2/g)**	V_{tot} **(mm^3_{liq}/g)**	V_{micro} **(mm^3_{liq}/g)**
CH-B	4.6 ± 0.1	– (*)	7	–
CH-ZnO	3.0 ± 0.2	–	–	–
CC-B	24.0 ± 1	14 ± 0.4	21	6
CC-ZnO	35.0 ± 1	15 ± 0.5	39	10

(*) volume of micropores below magnitudes accessible by the *t*-plot method (S_{meso} < 1 m^2/g, V_{micro} < 1 mm^3/g)

Table 2. Parameters of the models applied to equilibrium test data.

		Pb					As				
		Q_0 (mg/g)	K_L (L/mg)		χ^2	R^2	Q_0 (mg/g)	K_L (L/mg)		χ^2	R^2
Langmuir	**CH-B**	12.958	0.211		0.600	0.979	- (*)	-		-	-
	CH-ZnO	15.911 (**)	1.212		7.315	0.837	1.545	0.148		0.011	0.960
	CC-B	5.829	0.696		0.316	0.945	13.058	0.005		0.307	0.910
	CC-ZnO	94368.477 (**)	0.000		12.498	0.833	25.936	3.996		6.254	0.944
		K_F (mg/g)/(mg/L)^n	**n**		χ^2	R^2	K_F (mg/g)/(mg/L)^n	**n**		χ^2	R^2
Freundlich	**CH-B**	3.115	0.377		0.425	0.985	- (*)	-		-	-
	CH-ZnO	6.081 (**)	0.347		6.845	0.848	0.438	0.274		0.019	0.929
	CC-B	2.664	0.209		0.360	0.938	0.100	0.827		0.364	0.894
	CC-ZnO	34.520 (**)	1.544		7.643	0.898	16.186	0.202		13.360	0.880
		K_{RP} (L/g)	a_{RP} (mg/L)	**g**	χ^2	R^2	K_{RP} (L/g)	a_{RP} (mg/L)	**g**	χ^2	R^2
Redlech-Peterson	**CH-B**	9.217	1.907	0.741	0.153	0.996	- (*)	-	-	-	-
	CH-ZnO	31.220 (**)	3.348	0.799	7.805	0.861	0.362	0.390	0.889	0.010	0.970
	CC-B	15.223	4.279	0.870	0.276	0.960	0.066	0.005	1.000	0.410	0.910
	CC-ZnO	0.389 (**)	-0.989	0.008	9.555	0.894	108.319	4.291	0.987	7.468	0.944
		q_{DR} (mg/g)	k_{DR} (mol^2/kJ^2)		χ^2	R^2	q_{DR}	k_{DR}		χ^2	R^2
Dubinin-Radushkevich	**CH-B**	9.769	0.235		4.369	0.844	- (*)	-		-	-
	CH-ZnO	14.642 (**)	0.084		6.988	0.845	1.376	5.197		0.015	0.732
	CC-B	5.476	0.379		0.486	0.916	4.885	193.235		0.167	0.951
	CC-ZnO	51.784 (**)	0.186		6.496	0.913	24.363	0.034		7.205	0.935

(*) Data not reported because of very low values and randomness of the datapoints
(**) The equilibrium was not reached
The initial (before addition of adsorbent) and final (after 48 h) pH levels were measured for every concentration and showed in the table S4.

Table 3. Parameters of the models applied to Kinetic test data.

		Pb				As			
		q_e (mg/g)	k_1 (min^{-1})	χ^2	R^2	q_e (mg/g)	k_1 (min^{-1})	χ^2	R^2
PFO	**CH-B**	3.249	0.050	0.213	0.862	2.867	0.021	0.054	0.960
	CH-ZnO	13.785	0.097	0.768	0.973	4.117	0.025	0.125	0.950
	CC-B	8.108	0.011	0.270	0.966	1.703	0.113	0.064	0.898
	CC-ZnO	16.208	0.360	2.013	0.932	8.847	0.081	1.321	0.878
		q_e (mg/g)	k_2 (g/mg.min)	χ^2	R^2	q_e(mg/g)	k_2 (g/mg.min)	χ^2	R^2
PSO	**CH-B**	3.604	0.020	0.113	0.927	3.459	0.007	0.028	0.979
	CH-ZnO	15.004	0.009	0.097	0.997	4.878	0.006	0.051	0.979
	CC-B	10.753	0.001	0.225	0.972	1.989	0.062	0.061	0.903
	CC-ZnO	16.995	0.034	0.516	0.983	9.622	0.012	0.571	0.947
		a (mg/g.min)	b (mg/g)	χ^2	R^2	a (mg/g.min)	b (mg/g)	χ^2	R^2
Elovich	**CH-B**	0.698	1.523	0.032	0.979	0.122	1.160	0.017	0.988
	CH-ZnO	6.563	0.407	0.712	0.975	0.243	0.890	0.009	0.996
	CC-B	0.140	0.319	0.184	0.977	0.660	2.652	0.004	0.973
	CC-ZnO	1065.901	0.664	0.468	0.984	4.279	0.644	0.040	0.996
		K_p ($mg/g.min^{0.5}$)	C (mg/g)	χ^2	R^2	K_p ($mg/g.min^{0.5}$)	C (mg/g)	χ^2	R^2
Intraparticle model	**CH-B**	0.222	0.688	0.109	0.929	0.222	0.688	0.109	0.929
	CH-ZnO	0.869	4.247	6.309	0.776	0.869	4.247	6.309	0.776
	CC-B	0.519	-0.090	0.126	0.984	0.519	-0.090	0.126	0.984
	CC-ZnO	0.741	8.813	13.562	0.540	0.741	8.813	13.562	0.540

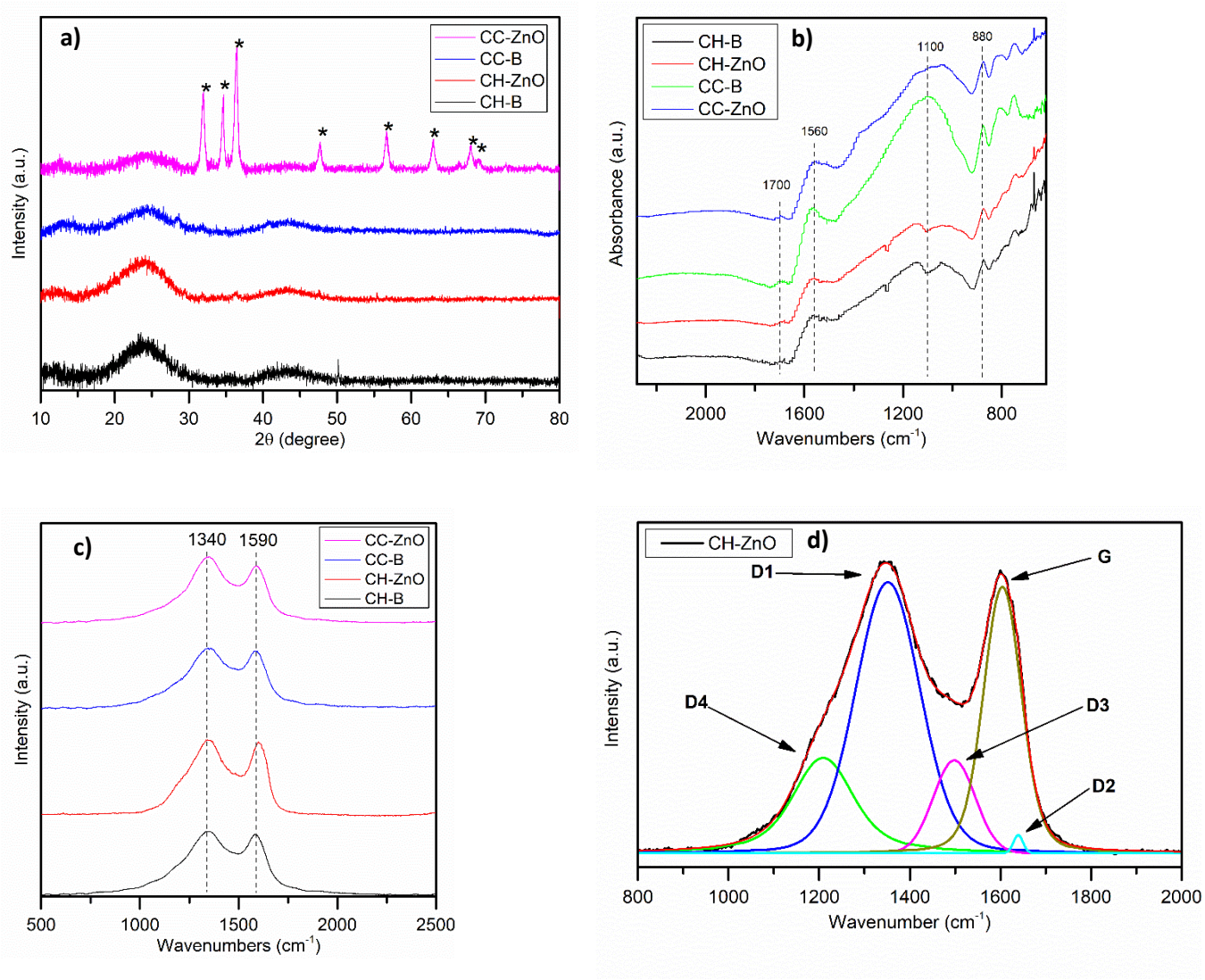
a)
CC-ZnO
CC-B
CH-ZnO
CH-B
Intensity (a.u.)
2θ (degree)
b)
CH-B
CH-ZnO
CC-B
CC-ZnO
1700
1560
1100
880
Absorbance (a.u.)
Wavenumbers (cm-1)
c)
1340
1590
CC-ZnO
CC-B
CH-ZnO
CH-B
Intensity (a.u.)
Wavenumbers (cm-1)
CH-ZnO
d)
D1
G
D4
D3
D2
Intensity (a.u.)
Wavenumber (cm-1)

Figure 1.

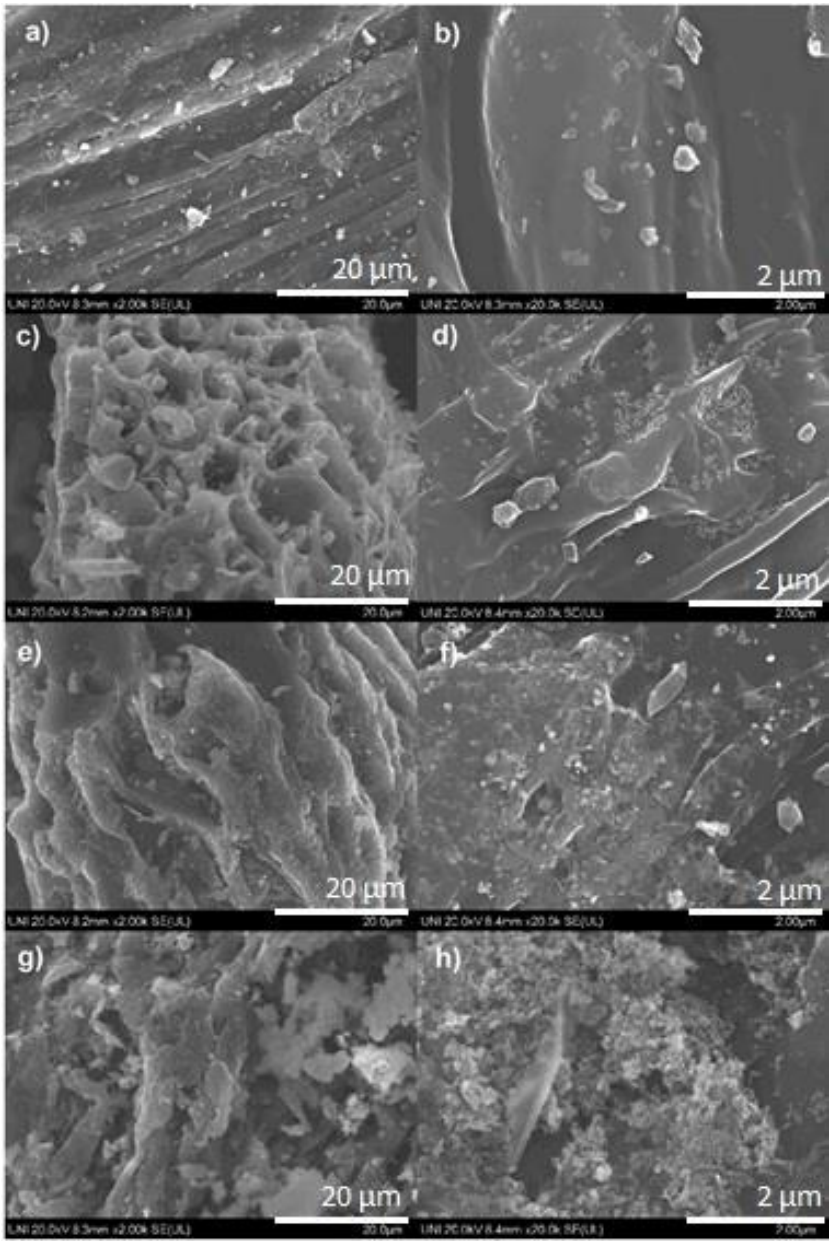

Figure 2.

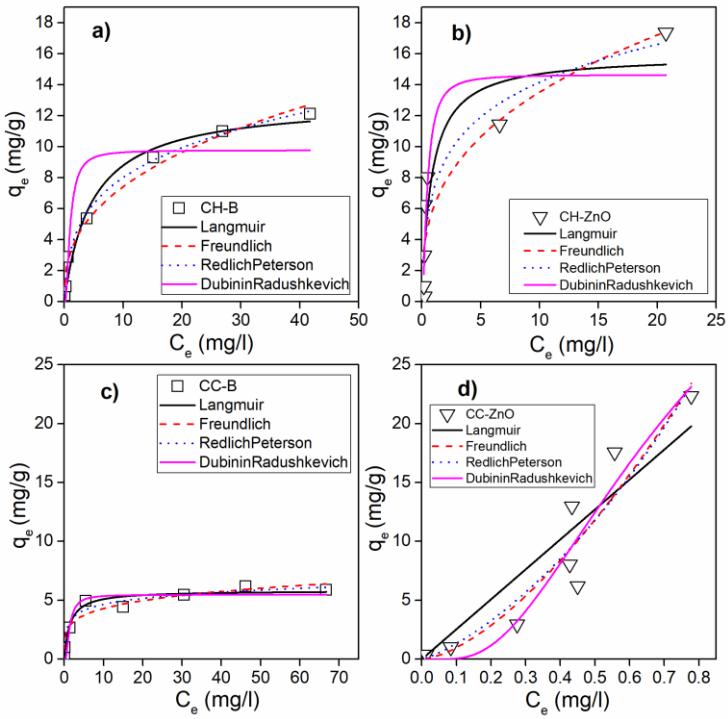
a)
b)
c)
d)
CH-B
CH-ZnO
CC-B
CC-ZnO
Langmuir
Freundlich
RedlichPeterson
DubininRadushkevich
q_e (mg/g)
C_e (mg/l)

Figure 3.

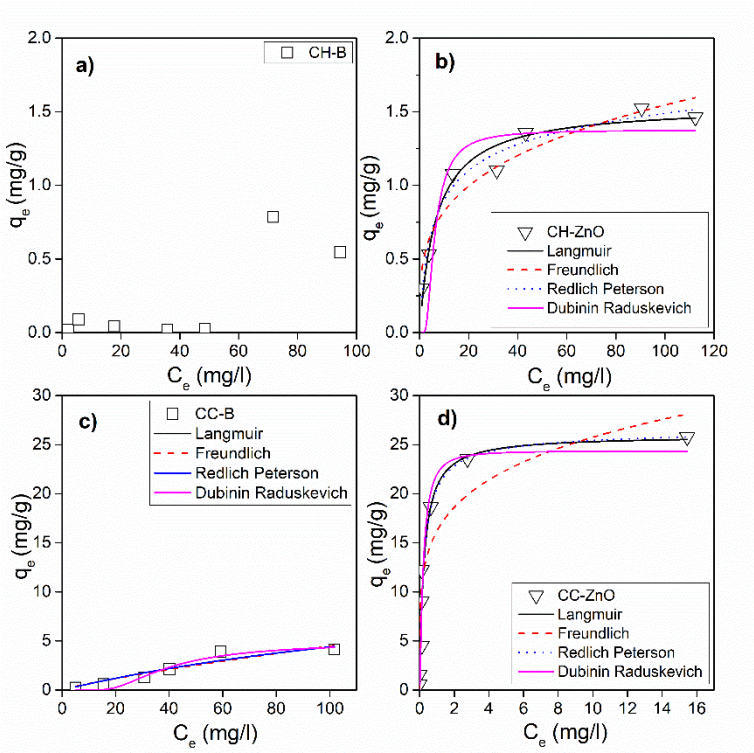
a)
CH-B
b)
CH-ZnO
Langmuir
Freundlich
Redlich Peterson
Dubinin Raduskevich
c)
CC-B
Langmuir
Freundlich
Redlich Peterson
Dubinin Raduskevich
d)
CC-ZnO
Langmuir
Freundlich
Redlich Peterson
Dubinin Raduskevich
q_e (mg/g)
C_e (mg/l)

Figure 4.

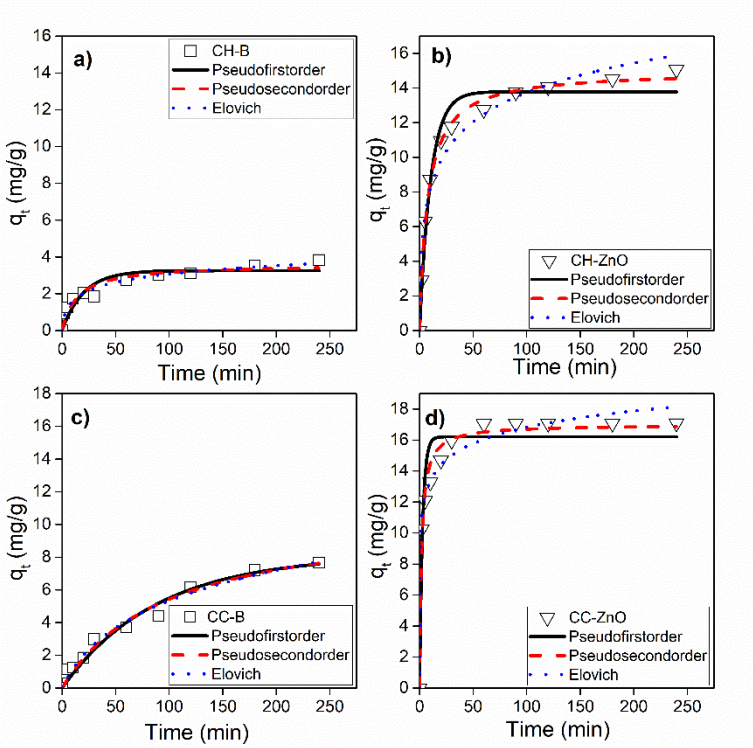
a)
CH-B
Pseudofirstorder
Pseudosecondorder
Elovich
b)
CH-ZnO
Pseudofirstorder
Pseudosecondorder
Elovich
c)
CC-B
Pseudofirstorder
Pseudosecondorder
Elovich
d)
CC-ZnO
Pseudofirstorder
Pseudosecondorder
Elovich
q_t (mg/g)
Time (min)

Figure 5.

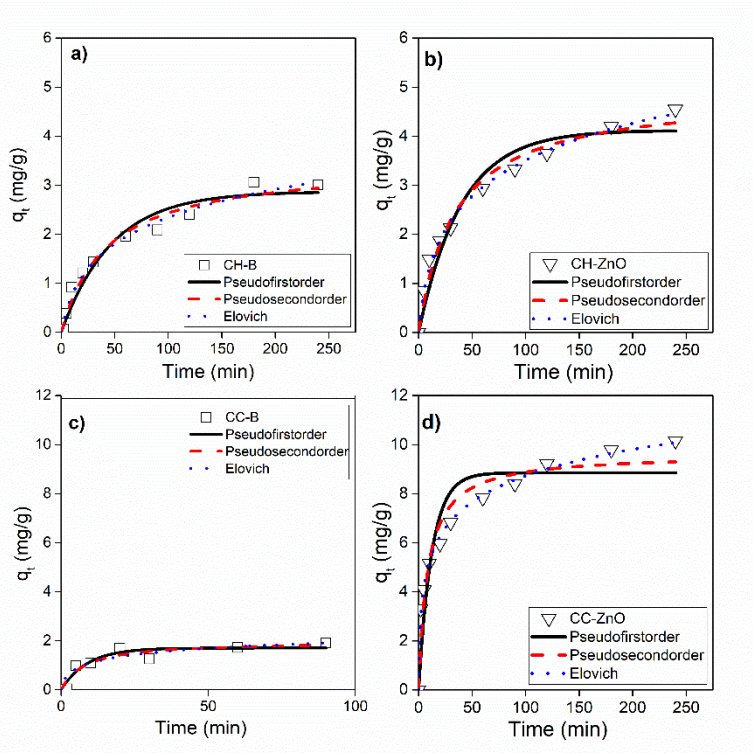
a)
b)
c)
d)
CH-B
CH-ZnO
CC-B
CC-ZnO
Pseudofirstorder
Pseudosecondorder
Elovich
q_t (mg/g)
Time (min)

Figure 6.

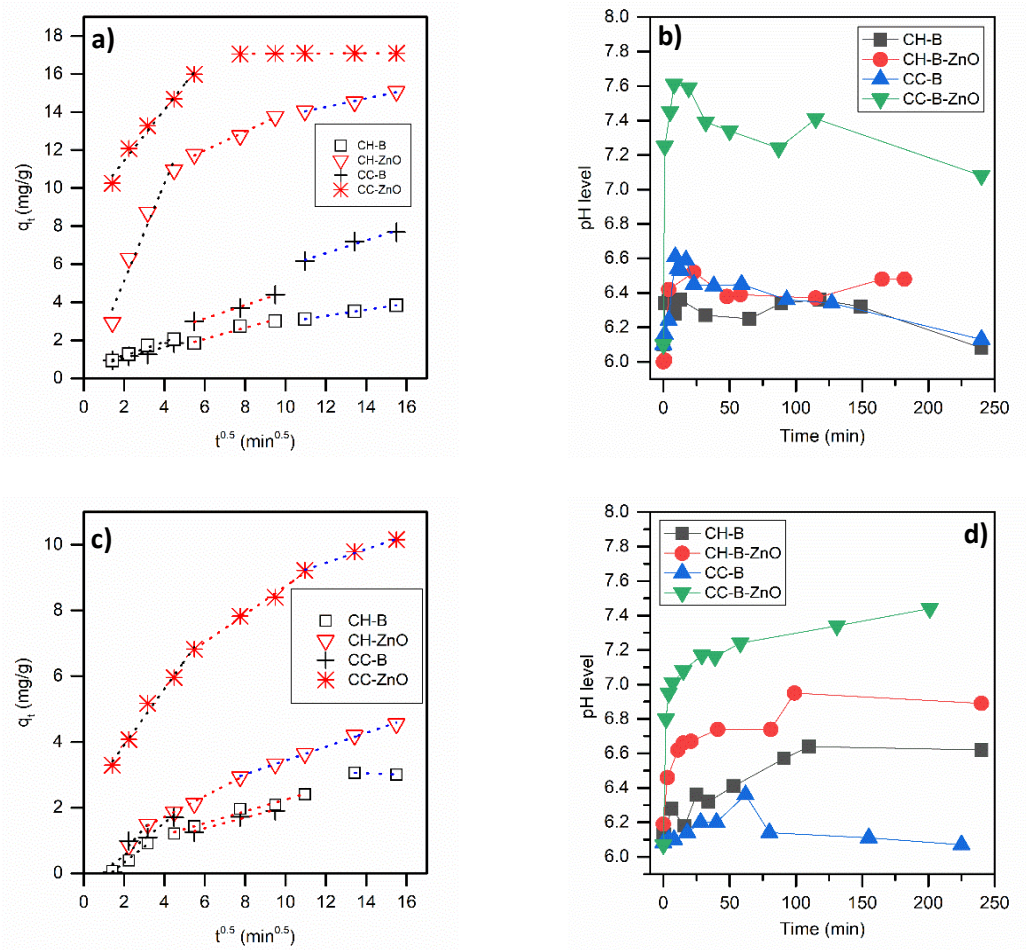
a)
b)
c)
d)
CH-B
CH-ZnO
CC-B
CC-ZnO
CH-B-ZnO
CC-B-ZnO
q_t (mg/g)
$t^{0.5}$ ($min^{0.5}$)
pH level
Time (min)

Figure 7.